nature electronics

Article

https://doi.org/10.1038/s41928-022-00880-1

Tailoring the magnetic exchange interaction in $MnBi_2Te_4$ superlattices via the intercalation of ferromagnetic layers

Received: 31 December 2021

Accepted: 27 October 2022

Published online: 12 December 2022

Check for updates

Peng Chen[1,2,3,17], Qi Yao[4,5,17] ✉, Junqi Xu[6], Qiang Sun[7,8], Alexander J. Grutter[9], Patrick Quarterman[9], Purnima P. Balakrishnan[9], Christy J. Kinane[10], Andrew J. Caruana[10], Sean Langridge[10], Ang Li[11], Barat Achinuq[12], Emily Heppell[12], Yuchen Ji[4,5], Shanshan Liu[13], Baoshan Cui[14,15], Jiuming Liu[1], Puyang Huang[1], Zhongkai Liu[4,5], Guoqiang Yu[14,15], Faxian Xiu[13], Thorsten Hesjedal[12], Jin Zou[7,8], Xiaodong Han[11], Haijun Zhang[6,16], Yumeng Yang[1] ✉ & Xufeng Kou[1,4] ✉

The intrinsic magnetic topological insulator $MnBi_2Te_4$ (MBT) provides a platform for the creation of exotic quantum phenomena. Novel properties can be created by modification of the $MnBi_2Te_4$ framework, but the design of stable magnetic structures remains challenging. Here we report ferromagnet-intercalated $MnBi_2Te_4$ superlattices with tunable magnetic exchange interactions. Using molecular beam epitaxy, we intercalate ferromagnetic MnTe layers into $MnBi_2Te_4$ to create $[(MBT)(MnTe)_m]_N$ superlattices and examine their magnetic interaction properties using polarized neutron reflectometry and magnetoresistance measurements. Incorporation of the ferromagnetic spacer tunes the antiferromagnetic interlayer coupling of the $MnBi_2Te_4$ layers through the exchange-spring effect at $MnBi_2Te_4$/MnTe hetero-interfaces. The MnTe thickness can be used to modulate the relative strengths of the ferromagnetic and antiferromagnetic order, and the superlattice periodicity can tailor the spin configurations of the synthesized multilayers.

In magnetic topological insulators (MTIs), the coexistence of broken time-reversal symmetry and topologically non-trivial surface states gives rise to a variety of time-reversal symmetry-breaking physics[1–6]. To obtain robust ferromagnetism in MTIs, transition-metal elements (Cr, V, Mn) are typically incorporated into the host topological insulator matrix[2,7,8]. However, the random distribution of magnetic atoms leads to a spatial fluctuation of the magnetic exchange gap, which restricts MTI-related phenomena to deep cryogenic temperatures[9]. One way to address this challenge is to design TI-based magnetic heterostructures in which uniform magnetic order is induced via the interfacial proximity effect[10,11]. In this approach, separate layers control the topological and magnetic behaviours of the heterostructure, so their contributions can be tuned independently. However, critical lattice-matching requirements limit the selection of TI-compatible magnetic films, and only a few MTI heterostructures have been successfully fabricated so far[11–13].

$MnBi_2Te_4$ (MBT) is an intrinsic MTI material[14–16]. The covalently bonded manganese atoms form a two-dimensional (2D) lattice plane within the stacked Te–Bi–Te–Mn–Te–Bi–Te septuple layers (SLs)[17,18]. This septuple structure preserves the large spin–orbit coupling required for band inversion, and provides a homogeneous magnetic ground state with intra-layer ferromagnetism (FM) and interlayer A-type anti-ferromagnetism (AFM)[17]. As a result, dissipationless chiral edge conduction has been observed in thin MBT flakes above 1 K,

A full list of affiliations appears at the end of the paper. ✉e-mail: yaoqi@shanghaitech.edu.cn; yangym1@shanghaitech.edu.cn; kouxf@shanghaitech.edu.cn

https://doi.org/10.1038/s41928-022-00880-1

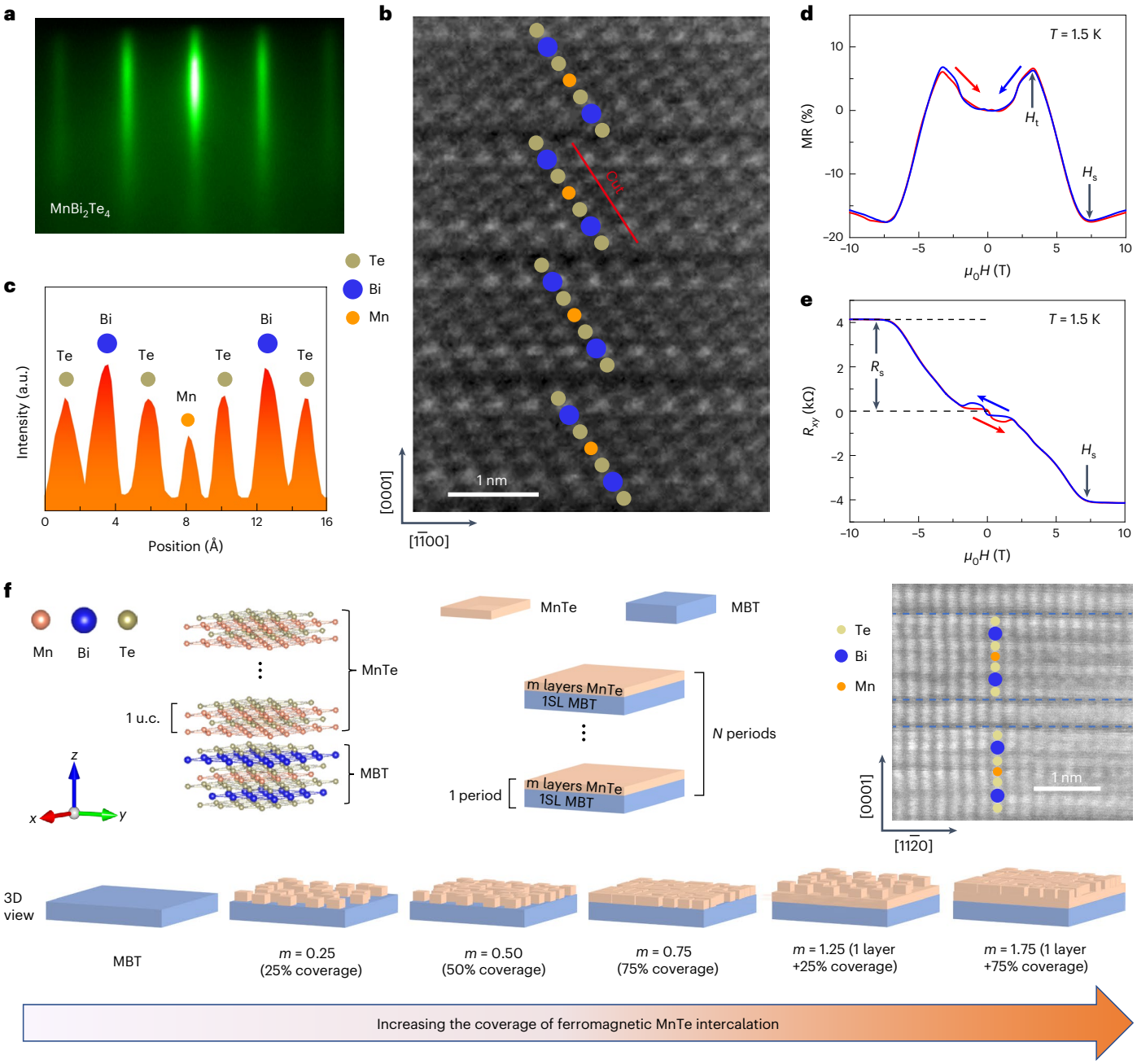

Fig. 1 | Structural and electrical characterizations of the MBE-grown MBT thin film. a, In situ RHEED with a sharp streaky pattern reveals the epitaxial growth mode. **b**, Cross-sectional HR-STEM image of the MBT film grown on the Al_2O_3 (0001) substrate. **c**, Intensity distribution mapping along the cut marked in **b**. **d**,**e**, Magnetic field-dependent MR (**d**) and R_{xy} (**e**) data of the 5-SL MBT sample. Both the AFM-type GMR line shape and spin-flop-induced hysteresis loop at 1.5 K are consistent with bulk MBT data. **f**, Schematic of the FM-intercalated [(MBT)$(MnTe)_m]_N$ structure and the relevant HR-STEM image. The blue dashed lines indicate the MBT/MnTe interfaces in the superlattice structure. By varying the intercalated MnTe layer coverage (m) and superlattice repeats (N), the magnetic exchange interactions can be regulated. u.c., unit cell.

although it requires the presence of a large external magnetic field to fully magnetize the samples[14,19,20].

Through modification of the MBT framework, spontaneous magnetization at zero magnetic field has been achieved[14]. Recent attempts to insert a Bi_2Te_3 spacer into MBT has produced the (MBT)$(Bi_2Te_3)_n$ (n = 1–6) series of superlattices, where the interlayer AFM-type Anderson super-exchange coupling strength is reduced dramatically with increasing n (refs. [21–25]). However, this non-magnetic intercalation strategy can cause unintended magnetic fluctuations[26]. The $Mn_2Bi_2Te_5$ system was proposed as a candidate to improve the magnetic stability of the original MBT SL due to the additional Mn layer in the Mn–Te double spacer. However, the Mn atoms tend to dope into MBT rather than form a stable Mn–Te–Mn structure during the $Mn_2Bi_2Te_5$ single-crystal growth[17], and the development of FM-intercalated MBT remains elusive[27].

In this Article we report ferromagnet-intercalated MBT superlattices. Using molecular beam epitaxy (MBE), we have grown [(MBT)$(MnTe)_m]_N$ superlattices with fixed MBT thickness as one SL within each period, in which m is the nominal MnTe layer coverage and N is the number of superlattice periods. The insertion of the MnTe spacer

https://doi.org/10.1038/s41928-022-00880-1

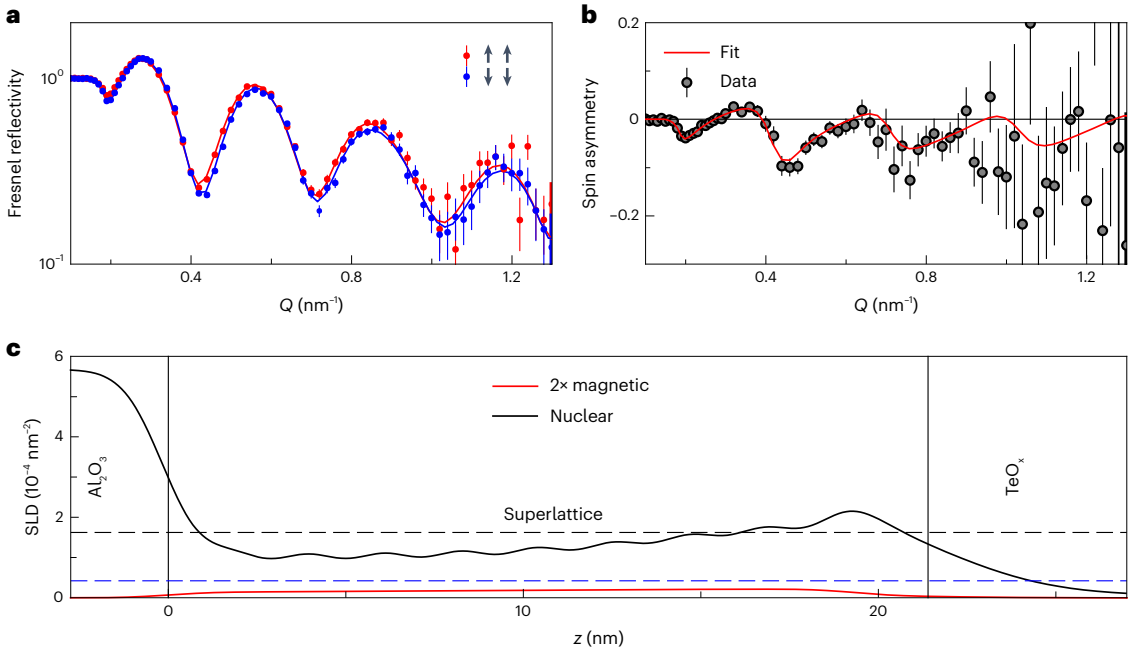

Fig. 2 | Polarized neutron reflectometry measurements on the MBE-grown [(MBT)(MnTe)$_{1.75}$]$_{10}$ superlattice. a,**b**, Polarized neutron reflectivities (**a**) and spin asymmetry (**b**) alongside theoretical curves for the Te-capped [(MBT)(MnTe)$_{1.75}$]$_{10}$ sample. **c**, Best-fit nuclear and magnetic SLD profile used to generate the theoretical curves. All error bars shown in this figure represent ±1 s.d. and are based on counting statistics for each point. Measurements were performed at T = 6 K under a 3-T in-plane applied magnetic field. The black dashed line represents the expected bulk nuclear SLD of the MBT component, and the blue dashed line corresponds to the ideal bulk nuclear SLD of MnTe. The depth-average magnetization of ~30 e.m.u. cc^{-1} (averaged over the whole superlattice) is obtained from the PNR data.

with perpendicular FM order tunes the relative AFM-to-FM strength and stabilizes the interlayer exchange coupling between the MBT layers. Furthermore, by controlling the superlattice periodicity, we can manipulate the spin texture of the entire superlattice structure with configurable magnetoresistance (MR) responses.

Structural and magnetic properties of MBT and [(MBT)(MnTe)$_m$]$_N$ samples

We first grew MBT thin films by depositing individual MnTe and Bi_2Te_3 layers on 2-inch Al_2O_3(0001) substrates in an alternating sequence, followed by a moderate post-annealing procedure to form the MBT SL structure. The absence of dangling bonds on the Al_2O_3 surface promotes the epitaxial growth of MBT, and the sharp streaky pattern found by in situ reflection high-energy electron diffraction (RHEED) shows a 2D growth mode of the as-grown MBT films (Fig. 1a). The cross-sectional high-resolution scanning transmission electron microscopy (HR-STEM) image of the MBT specimen in Fig. 1b clearly demonstrates the highly ordered atomic distribution of the desired Te–Bi–Te–Mn–Te–Bi–Te sequence. Quantitative analysis of the intensity distribution in Fig. 1c confirms an elemental composition ratio of Mn:Bi:Te = 1:2:4 in the single-crystalline thin film, and the X-ray diffraction (XRD) pattern in Supplementary Section 1 exhibits a series of (00n) peaks without observable secondary phases; both results agree well with the ideal stoichiometric MBT values. Additionally, polarized neutron reflectometry (PNR) measurements of the Te-capped MBT film reveal a nuclear scattering length density (SLD) profile consistent with bulk-like MBT. Furthermore, the magnetic SLD depth profile exhibits a uniform magnetization distribution across the film, with a magnitude in accordance with that expected from MBT in an in-plane magnetic field, evidencing the high-quality growth of the designed phase (Supplementary Fig. 2-1 and Supplementary Section 2).

We next performed six-point magneto-transport experiments on the 5-SL MBT sample to explore its magnetic/electrical properties. Consistent with studies of exfoliated MBT flakes[14,19,28], the MR displays a hump-like line shape at T = 1.5 K, as highlighted in Fig. 1d. In particular, the initial antiparallel alignment of spins in adjacent MBT layers leads to the high-MR state in the low-magnetic-field region, and the abrupt increase in magnitude to an MR peak near a field of ±3.3 T (defined as the transition field, H_t) corresponds to the characteristic spin-flop feature for an A-type AFM system[14,19,28]. On further increasing the applied magnetic field, all magnetic moments become polarized along the z direction at a saturation field of H_s = 7 T, and the MBT sample falls into a low-MR state. This behaviour is similar to the giant magnetoresistance (GMR) effect found in a spin-valve system (details of the GMR model are discussed in Supplementary Section 3). As long as the Mn:Bi:Te element ratio is accurately tuned, the corresponding anomalous Hall resistance (R_{xy}) (Fig. 1e) reaches its saturation value of R_s = 4 kΩ, which is higher than for the Bi_2Te_3-excess and MnTe-excess MBT counterparts (Supplementary Section 4). Note that the hybrid-anomalous Hall effect (AHE)-like R_{xy} slope at low magnetic fields (±3.3 T) may be caused by native anti-site defects and/or random stacking order in the MBT, which in turn modify the local electronic structures and magnetic moments[25,27,29]. From the aforementioned structural and electrical characterizations, we have validated the high quality of our MBT layer as a reliable building block for the following study.

Based on our previous experience with growing FM-phase MnTe film[30], we chose it as the intercalated layer when creating the [(MBT)(MnTe)$_m$]$_N$ system. As illustrated in Fig. 1f, by carefully choosing an appropriate substrate temperature window and a moderate post-annealing process (Methods), the similar 2D stoichiometric structures and negligible lattice mismatch of the FM-phase α-MnTe and MBT guarantee epitaxial growth of the designed superlattice structure, where the strong perpendicular ferromagnetism (Curie temperature of T_C ≈ 150 K) of MnTe can add robust FM interactions to the hybrid system (Supplementary Fig. 5), and the surface coverage of the MnTe spacer between adjacent MBT layers m (statistically equal to the total growth time for the MnTe layer divided by that of one MnTe unit cell)

https://doi.org/10.1038/s41928-022-00880-1

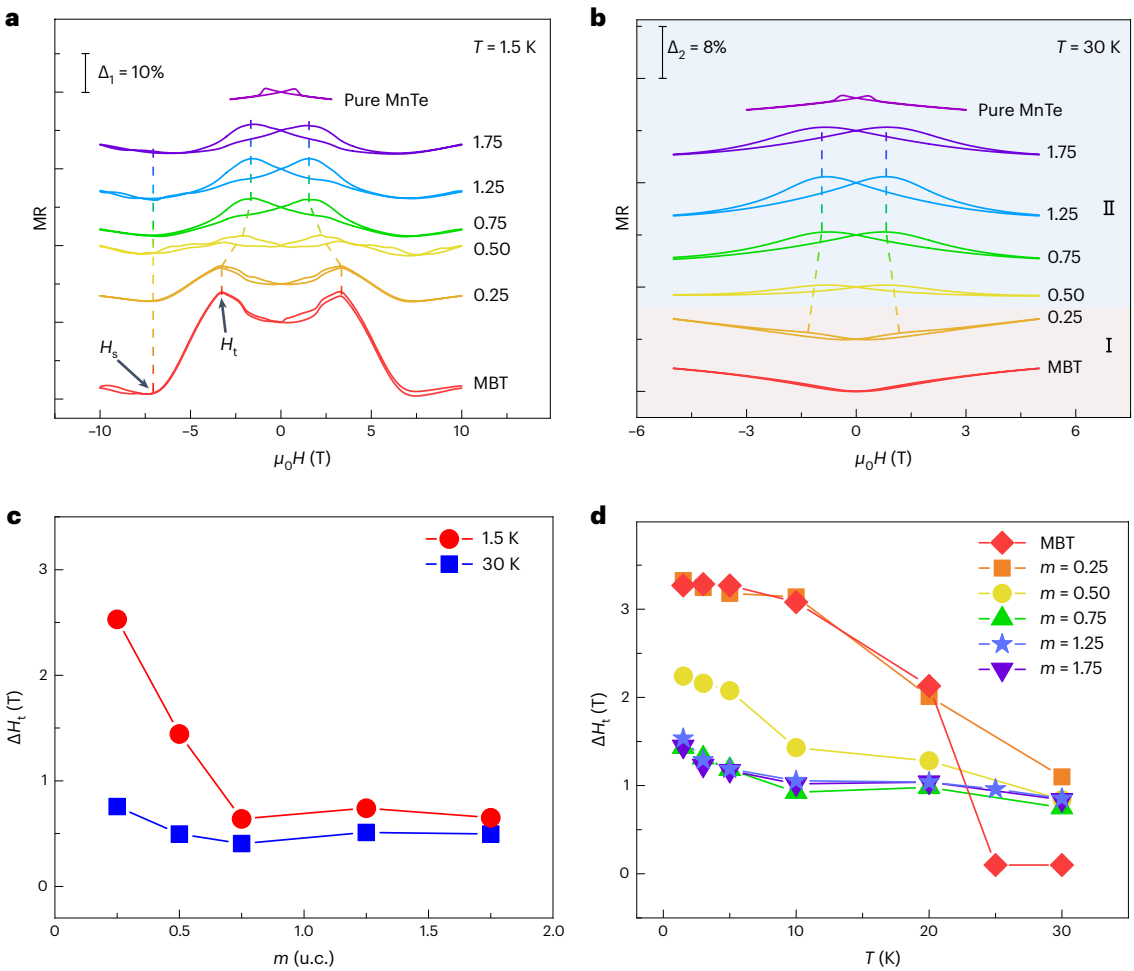

Fig. 3 | Manipulation of the exchange-spring effect in [(MBT)(MnTe)$_m$]$_5$ samples through MnTe intercalation. a,**b**, MnTe spacer thickness-dependent MR curves at $T = 1.5$ K (**a**) and $T = 30$ K (**b**). The value of m varies from 0 to 1.75. Data are shifted vertically by Δ_1 and Δ_2 for convenient comparison, and positive and negative MR regions are labelled by coloured areas I and II, respectively. **c**, Evolution of ΔH_t with respect to MnTe thickness. The negative correlation between ΔH_t and m at 1.5 K (red circles) reflects the exchange-spring effect, and the constant ΔH_t values at 30 K (blue squares) confirm the absence of AFM order in the system above the Néel temperature. **d**, The temperature-dependent H_t traces of the [(MBT)(MnTe)$_m$]$_5$ samples exhibit a clear MBT-to-MnTe transition feature at low temperatures.

can, in principle, be utilized to tune the interlayer AFM coupling[31,32]. It is noteworthy that the maximum thickness of the MnTe layer in this study is limited to below 1.34 nm (that is, two MnTe layers), which is sufficiently thin to ensure effective couplings among MBT layers in the superlattice[26,33].

Given the known tendency of Mn to diffuse extensively in MBT-related systems, we also performed neutron reflectometry experiments to directly probe the depth-resolved magnetization profiles of the [(MBT)(MnTe)$_m$]$_N$ superlattices. First, an unpolarized measurement of a nominal $m = 1.75$ sample with $N = 10$ superlattice repeats yielded an experimental MnTe layer coverage of $m = 1.72$, well within the experimental uncertainty of the expected value (Supplementary Fig. 2-2). Together with the appearance of the anticipated superlattice first-order Bragg reflection peak at a very high reciprocal lattice vector of $Q \approx 2.7$ nm^{-1}, this confirms the realization of a large-area, highly periodic [(MBT)(MnTe)$_{1.75}$]$_{10}$ structure by means of MBE (Supplementary Fig. 2-2a). An additional PNR measurement was conducted at $T = 6$ K under an applied in-plane magnetic field of 3 T. Figure 2a,b summarizes the best-fit results of the non-spin-flip reflectivities as well as the measured and theoretical spin asymmetry (defined as the difference between the spin-dependent reflectivities normalized by their sum) in reference to the desired [(MBT)(MnTe)$_{1.75}$]$_{10}$ superlattice structure. Although the measurement did not reach the first-order Bragg reflection due to the lower intensity of the polarized neutron beam, the oscillatory SLD depth profile in Fig. 2c describes the data well and is in line with periodic superlattice formation, with an average amplitude between the values of bulk MBT and MnTe. Moreover, compared with the pure 6-SL MBT data (Supplementary Fig. 2-1c), the integrated magnetic moment of the [(MBT)(MnTe)$_{1.75}$]$_{10}$ sample detected by PNR suggests a net contribution to the magnetization from the incorporated MnTe layers. Assuming that the MBT moment itself does not increase progressively with the applied field, our PNR results indicate a canted spin configuration with a non-zero in-plane magnetization of 30 e.m.u. cc^{-1} (note that this value is higher than that expected from the MnTe layer alone[34]) that may originate from the interplay between the MBT and MnTe layers via interfacial and interlayer exchange interactions.

Interlayer coupling mediated by the MnTe intercalation

To investigate the influence of MnTe intercalation we carried out temperature-dependent MR measurements on a set of [(MBT)(MnTe)$_m$]$_5$ samples, with m varying from 0 to 1.75 (Fig. 3). When the samples were cooled to $T = 1.5$ K (below the Néel temperature of MBT,

https://doi.org/10.1038/s41928-022-00880-1

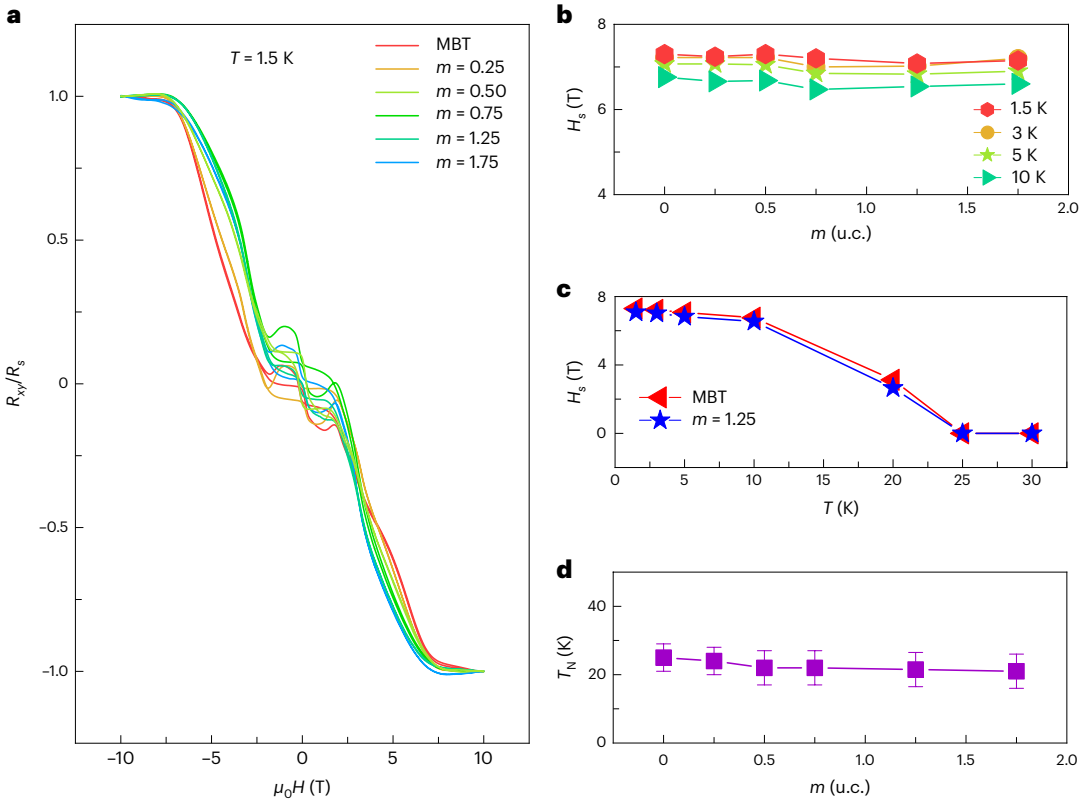

Fig. 4 | Mediation of interlayer couplings in the [(MBT)(MnTe)$_m$]$_5$ system. **a**, m-dependent anomalous Hall curves at $T = 1.5$ K. All samples show the same spin-flop behaviour, regardless of MnTe thickness. **b**, The extracted transition field H_s is insensitive to m at different temperatures. **c**, Temperature-dependent H_s curve of the [(MBT)(MnTe)$_{1.25}$]$_5$ superlattice as compared with the pure 5-SL MBT control sample ($m = 0$). **d**, The Néel temperature, T_N, remains almost unchanged in all [(MBT)(MnTe)$_m$]$_5$ samples, indicating the stabilization effect by the MnTe intercalation.

$T_N = 25$ K; ref. [16]), the MR signals exhibited a strong dependence on m. As shown in Fig. 3a, the MR peak transition field H_t monotonically shrinks with increasing MnTe thickness (that is, the change in H_t compared to the pure FM-phase MnTe film (ΔH_t) successively decreases from 3.3 T ($m = 0.25$) to 1.4 T ($m = 1.75$) at $T = 1.5$ K), indicating effective modulation of the exchange-spring effect through MnTe intercalation. Meanwhile, the dramatic decrease of MR amplitude from $m = 0$ (16%) to $m = 0.5$ (2.65%) implies suppression of the AFM-related GMR component by the introduced FM order. By further increasing m, the contribution of the MnTe layer becomes more pronounced, triggering the appearance of a double-split butterfly MR response from its original curve. Eventually, the overall MR profile of the MnTe-dominated superlattice system ($m \geq 0.75$) resembles that of the pure MnTe control sample, except for a larger transition field (H_t). In fact, similar exchange-spring magnet-like MR behaviours are also observed in conventional magnetic multilayers (for example, in NiFe/IrMn and NiFe/Co stacks)[32,35]. Depending on the relative strengths of the anisotropy and exchange coupling energy between the magnetic components, the ground-state spin texture of the system and its correlated magneto-transport responses can be tuned[31,36]. In our MnTe-intercalated MBT superlattices, when the soft magnet MnTe couples with the magnetically hard MBT single layer, the strong anisotropy of the latter can pin the magnetic moment within the MnTe layer via magnetic proximity coupling at the interface[37–41], resulting in an enlarged H_t. On the other hand, as the base temperature is elevated above the T_N of MBT, the absence of the AFM-type interlayer Anderson super-exchange coupling drives the pure 5-SL MBT sample into a paramagnetic state, as verified by the positive, parabolic MR curve detected at 30 K (the MBT curve of Fig. 3b). With increasing MnTe thickness, the MR curves show a transition from positive (coloured area I) to negative (coloured area II) and, subsequently, the entire magneto-transport behaviour of the [(MBT)(MnTe)$_m$]$_5$ system is only governed by the remaining MnTe-related FM order. Consequently, typical butterfly-shaped MR slopes with a constant peak position are recorded, and the trend of the corresponding ΔH_t is exhibited in Fig. 3c (blue squares), which is not affected by the MnTe thickness (that is, the same as for the pure FM-type MnTe film[30]). Furthermore, the temperature-dependent H_t slopes in Fig. 3d display a clear MBT-to-MnTe transition trait as m varies from 0.25 to 1.75, providing critical guidance in evaluating the competing intra-/interlayer magnetic couplings.

In addition to enabling coercivity modulation, the identified exchange-spring effect is found to stabilize the interlayer coupling between adjacent MBT layers in our [(MBT)(MnTe)$_m$]$_N$ superlattices. Unlike the m-dependent H_t phenomenon noted in the low-field region, the saturation field H_s, which characterizes the interlayer exchange coupling strength, remains constant at 7 T (that is, it has the same value as the non-intercalated MBT film) and shows a negligible variation with respect to m (Fig. 3a, straight dashed line). To understand this distinctive feature, we carried out high-field anomalous Hall resistance measurements on the same set of [(MBT)(MnTe)$_m$]$_5$ samples at low temperatures. It is worth noting that the normalized Hall resistance (defined as R_{xy}/R_s) curves at $T = 1.5$ K (Fig. 4a) show almost identical contours, indicating a universal transition process as the magnetic moments in the superlattice are gradually aligned by the applied field. In agreement with the MR results in Fig. 3, the H_s values extracted from the AHE data at $T = 1.5$, 3, 5 and 10 K also stay independent of MnTe spacer thickness (Fig. 4b). Similarly, the H_s–T slopes follow the same temperature-scaling trace up to 25 K (Fig. 4c), above which the interlayer AFM order disappears ($H_s = 0$) and the overall AHE signal reverts to that of a single-phase FM-driven R_{xy} hysteresis loop.

https://doi.org/10.1038/s41928-022-00880-1

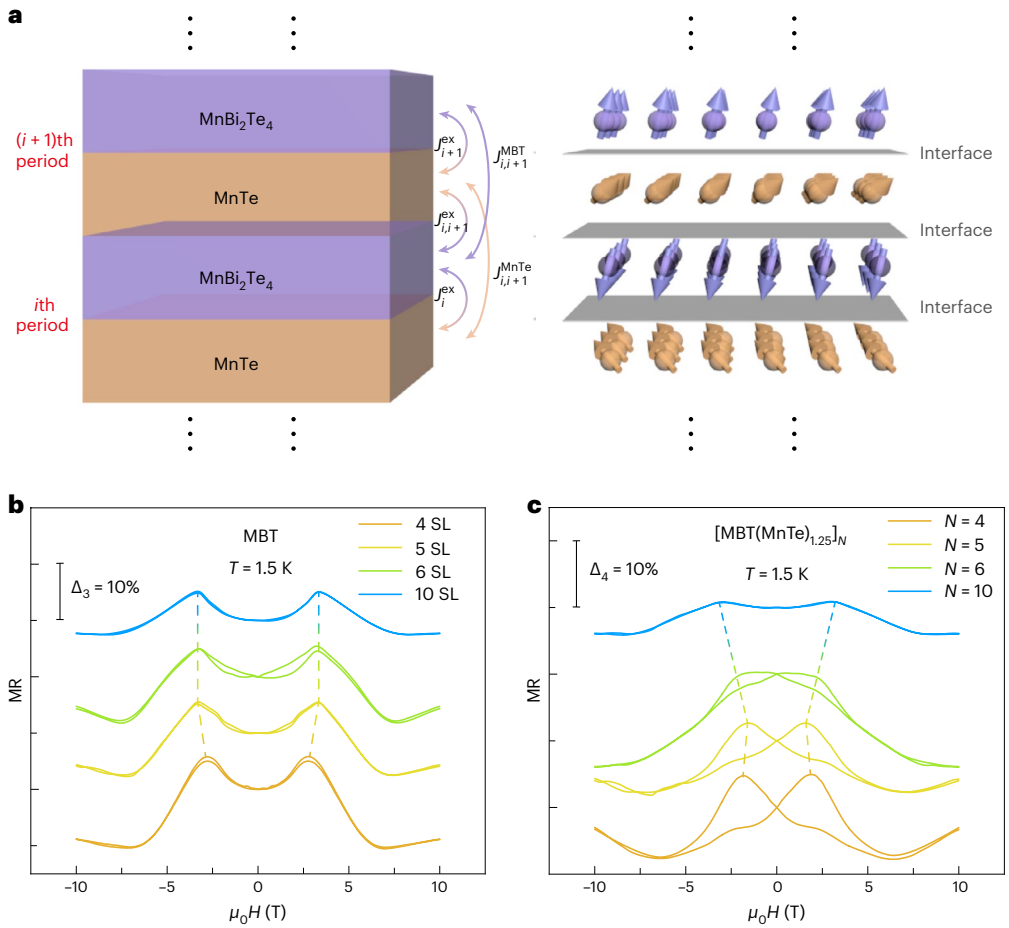

Fig. 5 | Tunable MR responses through superlattice engineering. **a**, Illustrations of the interfacial and interlayer exchange interactions (left) and the resulting canted spin configuration (right) for the $[(MBT)(MnTe)_m]_N$ superlattices based on the modified linear chain model simulation. The in-plane spin rotation is induced by J_i^{ex}. **b**,**c**, Evolutions of MR responses in thickness-dependent pure MBT thin films (**b**) and $[(MBT)(MnTe)_{1.25}]_N$ samples (**c**). As the number of superlattice repeats N increases from 4 to 10, the reinforced canted magnetization and long-range interactions drive the overall MR signal from the FM-dominated double-split butterfly shape towards the AFM-type GMR contour.

Modified linear chain model

Quantitatively, the distinct evolutions of H_t and H_s versus MnTe thickness can be well described by a modified linear chain model[42–44], in which the magnetization of each constituent MBT and MnTe layer is considered a 'macro spin'. As schematized in Fig. 5a, the magnetic interactions in the $[(MBT)(MnTe)_m]_N$ superlattice system consist of the exchange couplings between nearest-neighboured MBT-to-MBT, MnTe-to-MnTe and MBT-to-MnTe layers, respectively. Accordingly, the total energy E_N of the system can be expressed as a function of the applied magnetic field $\mathbf{H}$ (refs. [42–44]):

$$E_N\left(\mathbf{m}_i^{MBT}, \mathbf{m}_i^{MnTe}, \mathbf{H}\right) = \sum_{i=1}^{N-1}\Big[J_i^{MBT}\mathbf{m}_i^{MBT}\cdot\mathbf{m}_{i+1}^{MBT} + J_i^{MnTe}\mathbf{m}_i^{MnTe}\cdot\mathbf{m}_{i+1}^{MnTe} + \tilde{J}_i^{MBT}\left(\mathbf{m}_i^{MBT}\cdot\mathbf{m}_{i+1}^{MBT}\right)^2 + \tilde{J}_i^{MnTe}\left(\mathbf{m}_i^{MnTe}\cdot\mathbf{m}_{i+1}^{MnTe}\right)^2\Big] - \sum_{i=1}^{N} J_i^{ex}\mathbf{m}_i^{MBT}\cdot\mathbf{m}_i^{MnTe} - \sum_{i=1}^{N}\left[K_i^{MBT}t_i^{MBT}\left(\mathbf{m}_i^{MBT}\cdot\mathbf{z}\right)^2 + K_i^{MnTe}t_i^{MnTe}\left(\mathbf{m}_i^{MnTe}\cdot\mathbf{z}\right)^2\right] - \sum_{i=1}^{N}\left(M_i^{MBT}t_i^{MBT}\mathbf{m}_i^{MBT} + M_i^{MnTe}t_i^{MnTe}\mathbf{m}_i^{MnTe}\right)\cdot\mathbf{H} \quad (1)$$

where J_i^{MBT} and $\tilde{J}_i^{MBT}$ (J_i^{MnTe} and $\tilde{J}_i^{MnTe}$) are the bilinear and biquadratic interlayer exchange coupling constants between adjacent MBT (MnTe) layers, J_i^{ex} denotes the MBT/MnTe interfacial magnetic interaction, K_i^{MBT} (K_i^{MnTe}), t_i^{MBT} (t_i^{MnTe}), M_i^{MBT} (M_i^{MnTe}) and $\mathbf{m}_i^{MBT}$ ($\mathbf{m}_i^{MnTe}$) correspond to the uniaxial anisotropy constant, thickness, saturated magnetization and the unit vector of magnetization direction of the ith MBT (MnTe) layer, respectively. The third term accounts for the anisotropy energy, and the fourth term represents the field-induced Zeeman energy from the uncompensated moments. Under the exchange-spring interaction scenario, the intercalated MnTe acts as a soft FM mediating adjacent antiparallel-coupled MBT layers, and the impact of the ith MnTe spacer on the MBT pair (M_i^{MBT} and M_{i+1}^{MBT}) can be expressed as modifications of the effective interlayer exchange coupling (J_{eff}^{MBT}) and uniaxial anisotropy (K_{eff}^{MBT})[42]. Therefore, equation (1) can be further expressed in a simplified formula:

$$E = J_{eff}^{MBT}\left[\cos\left(\theta_i - \theta_{i+1}\right) + \beta\cos^2\left(\theta_i - \theta_{i+1}\right)\right] + K_{eff}^{MBT}t_i^{MBT}\left(\sin^2\theta_i + \xi\sin^2\theta_{i+1}\right) - H_z t_i^{MBT}\left(M_i^{MBT}\cos\theta_i + M_{i+1}^{MBT}\cos\theta_{i+1}\right) \quad (2)$$

where $\theta_i(\theta_{i+1})$ is the angle deviation between M_i^{MBT} (M_{i+1}^{MBT}) and the magnetic easy axis (that is, the z direction), β and ξ are introduced as the scaling factors of the biquadratic coupling and different anisotropy, and t_i^{MBT} is the MBT layer thickness (see Supplementary Section 6 for a detailed discussion). From this modified linear chain model, it can be found that the transition field H_t is affected by the K_{eff}^{MBT} value,

whereas the saturation field H_s is mainly decided by the J_{eff}^{MBT} magnitude (Supplementary Fig. 6). Consequently, to recapture the m-dependent MR behaviours observed in Fig. 3, our simulation results suggest that, on the one hand, the insertion of MnTe modulates the magnetic orientation and anisotropy of the MBT layer (that is, intra-layer MBT coupling), and the calculated ground-state magnetic configuration of the superlattice with canted spin-polarization (Fig. 5a, right) is consistent with the PNR data elucidated in Fig. 2 (that is, the reduction of the effective anisotropy energy K_{eff}^{MBT} caused by MnTe insertion is also justified by density functional theory (DFT) calculations, as discussed in Supplementary Section 7). On the other hand, the presence of MnTe-to-MnTe interlayer coupling and an induced MnTe/MBT interfacial interaction both help to preserve the effective interlayer MBT coupling strength (that is, $J_{eff}^{MBT} = f(J_i^{MnTe}, J_i^{MBT}, J_i^{ex})$) with constant H_s and T_N via the exchange-spring effect (Supplementary Sections 8 and 9)[31,45,46]. Here, we should point out that, once the MnTe spacer is replaced by a non-magnetic layer (for example, $(Bi_{1-x}Sb_x)_2Te_3$), the FM-associated exchange interactions are absent in the resulting $[(MBT)((Bi_{1-x}Sb_x)_2Te_3)_1]_N$ counterpart (as confirmed by magneto-transport and X-ray magnetic circular dichroism data in Supplementary Sections 10 and 11), leaving the interlayer MBT coupling determined exclusively by the Anderson super-exchange mechanism (that is, $J_{eff}^{MBT} = J_i^{MBT}$). Guided by the same underlying physics elaborated in the modified linear chain model, it has been reported in the $(MBT)(Bi_2Te_3)_n$ system that the negative correlation between the AFM-type J_i^{MBT} and the intercalation distance would also result in a rapid suppression of T_N and reduction of H_s with increasing n (refs. [20,22]).

Tuning the interlayer coupling by superlattice engineering

Finally, we show the manipulation of the magnetic/spin configuration in the $[(MBT)(MnTe)_m]_N$ superlattice system via structural engineering. In pure MBT thin films, because both the intra-layer FM and interlayer AFM strength are non-adjustable in the fixed crystalline structure, the overall MR profile always maintains its GMR-like line shape (Fig. 5b), with slightly enlarged H_t and H_s fields, as the MBT thickness varies from the 2D (4-SL) to quasi-3D (10-SL) region (sample thicknesses calibrated by X-ray reflectivity are described in Supplementary Section 12). The reduced GMR amplitude is possibly caused by the increased bulk conduction in thicker films[14,19]. In contrast, with insertion of the MnTe spacer, the magnetic proximity effect can reorient the magnetic moments at the MBT/MnTe interface[40,41,47]. In these circumstances, it is expected that a change in the number of superlattice repeats (that is, the number of hetero-interfaces) will introduce dimension-dependent features into the related magneto-transport results. Specifically, the emerging butterfly-type double-split MR curve in the thin $[(MBT)(MnTe)_{1.25}]_4$ sample with $H_t = 2$ T suggests the existence of a sizable FM moment that is comparable with the original AFM order in the MBT/MnTe/MBT/MnTe unit, similar to other FM/AFM multi-layer systems[48–50]. With increasing repeat number, the added J_i^{ex} at the hetero-interfaces promotes the exchange-spring effect, as emphasized by the enlarged H_t field in Fig. 5c. Given that the adjacent MBT coupling is mediated through the sandwiched MnTe layer, an increase in superlattice repeats will cement such long-range interactions and stabilize the new ground state. Along with the reinforced canted magnetization orientation, which modifies the interfacial spin scattering, it is therefore anticipated that a more prominent AFM-type GMR behaviour is obtained in the $N = 10$ sample[10,51].

Conclusions

We have reported the development of intrinsic MTIs with tunable magnetic interactions by intercalating a ferromagnetic MnTe layer into MBT. In our designed superlattice structures, the interfacial and interlayer magnetic exchange interactions offer an effective approach to shape the overall spin texture. The AFM-to-FM transition can also be controlled through the thickness of the MnTe layer and the superlattice repeat number. Insertion of the MnTe spacer modifies the magnetic orientation and anisotropy of the MBT, resulting in an exchange-spring effect that preserves the global AFM coupling between adjacent MBT layers. Furthermore, the MR response can be tailored via superlattice engineering, so such an approach provides an additional degree of freedom in the design of practical spintronic memory and sensor prototypes. With further exploration of the topological features embedded in the host MBT matrix, our designed $[(MBT)(MnTe)_m]_N$ superlattices could serve as an advanced platform for creating axion insulator states and MTI-based exotic quantum phenomena.

Methods

Sample fabrication and structural characterizations

The $[(MBT)(MnTe)_m]_N$ superlattice films were grown epitaxially on an $Al_2O_3(0001)$ substrate by MBE under a vacuum of 1×10^{-8} Pa. Before sample growth, the Al_2O_3 substrate was pre-annealed at 570 °C to remove absorbed contamination. During MBE growth, high-purity Mn and Bi atoms were evaporated from standard Knudsen cells, and Te was evaporated using a thermal cracker cell. The epitaxial growth of one-septuple $MnBi_2Te_4$ was achieved by alternating deposition of one monolayer of Bi_2Te_3 and one of MnTe (substrate temperatures of 200 °C and 370 °C, respectively), followed by a moderate post-annealing step at 390 °C for 3 min. To ensure the single-crystallinity of MBT with the correct Bi–Mn–Te ratio as well as precise control of MnTe coverage in the superlattice structures, the flux ratio of each element was carefully quantified by in situ beam flux monitoring. Meanwhile, the real-time growth conditions and as-grown surface atom configuration were monitored by reciprocal RHEED patterns. X-ray diffraction and reflectivity measurements were performed to verify the crystal structure and to calibrate the film thickness, and atomic-resolution structural characterization was performed by an aberration-corrected Hitachi HF5000 STEM/TEM system in high-angle annular dark-field (HAADF) STEM mode (operated at 200 kV) and an aberration-corrected FEI-Titan-TEM system (operated at 300 kV).

Transport measurements

The as-grown superlattices were etched into a six-probe Hall-bar geometry with dimensions of 2 mm × 1 mm. The electrodes were made by welding small pieces of In onto the contact areas. The magneto-transport measurements of the fabricated devices were performed with ^{4}He refrigerators (Oxford Teslatron PT system), and several experimental variables, such as temperature, magnetic field and lock-in frequency, were adjusted during the measurements. Multiple lock-in amplifiers and Keithley source meters (with an excitation a.c. current of $I = 1$ μA) were connected to the samples to enable precise four-point lock-in experiments.

Neutron reflectometry

Unpolarized neutron reflectometry measurements and polarized neutron reflectometry measurements were performed using the PBR instrument at the NIST Center for Neutron Research. Incident and scattered neutrons were polarized parallel or antiparallel to the direction of the applied magnetic field. Because of the 3-T applied field, no net perpendicular magnetization was expected in the plane of the film, so the spin-flip scattering cross-sections could be neglected. We measured the non-spin-flip scattering cross-sections as a function of Q, the momentum transfer vector along the film normal direction. The data were reduced using the reductus[52] software package. Further unpolarized neutron reflectometry measurements were performed using the POLREF (https://doi.org/10.5286/ISIS.E.RB2000244) instrument at the ISIS Neutron and Muon Source (https://www.isis.stfc.ac.uk/Pages/polref.aspx). Incident and scattered beams were unpolarized, and the reflectivity was measured at room temperature, well above any magnetic transition. All reflectivity analysis was performed using the Refl1D software package[53].

First-principles calculations

First-principles calculations were performed within DFT using the projector augmented wave (PAW) method[54] as implemented in the Vienna ab initio simulation package (VASP)[55,56]. The exchange-correlation functional was treated under the generalized gradient approximation (GGA)[57], and the energy cutoff for the plane-wave basis was set to 420 eV for all calculations. The system geometry was optimized under full relaxation with a total energy tolerance of 10^{-5} eV for both the bulk MBT and the MBT$(MnTe)_1$ intercalation compounds. The spin–orbit coupling effect was self-consistently included, and the 3*d* orbitals of Mn atoms was considered by the DFT+U approach[58] introduced by Dudarev et al.[59] with $U_{eff} = 5$ eV for all results in this work. We also used the optB86b-vdW functional proposed by Klimeš et al.[60] to describe the van der Waals interactions. Furthermore, to calculate the different interlayer magnetic configurations, we constructed $1 \times 1 \times 2$ supercells for all systems. The magnetic exchange coupling parameters and single-ion anisotropy parameters of both bulk MBT and MBT$(MnTe)_1$ were obtained using the Hamiltonian model proposed by Lado and others[61].

XMCD measurements

X-ray magnetic circular dichroism (XMCD) measurements were performed on beamline I10 (BLADE) at the Diamond Light Source. X-ray absorption spectroscopy spectra were recorded at the Mn $L_{2,3}$ edges between 630 and 670 eV using the surface-sensitive total electron yield (TEY) detection mode in an ultrahigh-vacuum environment (~10^{-10} mbar). The measurements were carried out in an applied out-of-plane field of up to 7 T at various temperatures, with the input X-rays under normal incidence. In addition, X-ray absorption spectra were recorded with right (σ^+) and left (σ^-) circularly polarized X-rays, and XMCD signals were obtained as their difference ($\sigma^+ - \sigma^-$).

Data availability

The data that support the plots within this paper and other findings of the study are available from the corresponding authors upon reasonable request.

References

1. Chang, C. Z. et al. Experimental observation of the quantum anomalous Hall effect in a magnetic topological insulator. *Science* **340**, 167–170 (2013).
2. Kou, X. et al. Scale-invariant quantum anomalous Hall effect in magnetic topological insulators beyond the two-dimensional limit. *Phys. Rev. Lett.* **113**, 137201 (2014).
3. Nomura, K. & Nagaosa, N. Surface-quantized anomalous Hall current and the magnetoelectric effect in magnetically disordered topological insulators. *Phys. Rev. Lett.* **106**, 166802 (2011).
4. Li, R., Wang, J., Qi, X.-L. & Zhang, S.-C. Dynamical axion field in topological magnetic insulators. *Nat. Phys.* **6**, 284–288 (2010).
5. He, K., Wang, Y. & Xue, Q.-K. Quantum anomalous Hall effect. *Natl Sci. Rev.* **1**, 38–48 (2013).
6. Tokura, Y., Yasuda, K. & Tsukazaki, A. Magnetic topological insulators. *Nat. Rev. Phys.* **1**, 126–143 (2019).
7. Kou, X. et al. Metal-to-insulator switching in quantum anomalous Hall states. *Nat. Commun.* **6**, 8474 (2015).
8. Winnerlein, M. et al. Epitaxy and structural properties of (V, Bi, Sb)$_2$Te$_3$ layers exhibiting the quantum anomalous Hall effect. *Phys. Rev. Mater.* **1**, 011201 (2017).
9. Lee, I. et al. Imaging Dirac-mass disorder from magnetic dopant atoms in the ferromagnetic topological insulator $Cr_x(Bi_{0.1}Sb_{0.9})_{2-x}Te_3$. *Proc. Natl Acad. Sci. USA* **112**, 1316–1321 (2015).
10. He, Q. L. et al. Tailoring exchange couplings in magnetic topological-insulator/antiferromagnet heterostructures. *Nat. Mater.* **16**, 94–100 (2017).
11. Katmis, F. et al. A high-temperature ferromagnetic topological insulating phase by proximity coupling. *Nature* **533**, 513–516 (2016).
12. Lang, M. et al. Proximity induced high-temperature magnetic order in topological insulator-ferrimagnetic insulator heterostructure. *Nano Lett.* **14**, 3459–3465 (2014).
13. Tang, C. et al. Above 400-K robust perpendicular ferromagnetic phase in a topological insulator. *Sci. Adv.* **3**, e1700307 (2017).
14. Deng, Y. et al. Quantum anomalous Hall effect in intrinsic magnetic topological insulator $MnBi_2Te_4$. *Science* **367**, 895–900 (2020).
15. Li, J. et al. Intrinsic magnetic topological insulators in van der Waals layered $MnBi_2Te_4$-family materials. *Sci. Adv.* **5**, eaaw5685 (2019).
16. Otrokov, M. M. et al. Prediction and observation of an antiferromagnetic topological insulator. *Nature* **576**, 416–422 (2019).
17. Gong, Y. et al. Experimental realization of an intrinsic magnetic topological insulator. *Chin. Phys. Lett.* **36**, 076801 (2019).
18. Otrokov, M. M. et al. Highly-ordered wide bandgap materials for quantized anomalous Hall and magnetoelectric effects. *2D Mater.* **4**, 025082 (2017).
19. Liu, C. et al. Robust axion insulator and Chern insulator phases in a two-dimensional antiferromagnetic topological insulator. *Nat. Mater.* **19**, 522–527 (2020).
20. Yan, J.-Q. et al. A-type antiferromagnetic order in $MnBi_4Te_7$ and $MnBi_6Te_{10}$ single crystals. *Phys. Rev. Mater.* **4**, 054202 (2020).
21. Wu, J. et al. Toward 2D magnets in the $(MnBi_2Te_4)(Bi_2Te_3)_n$ bulk crystal. *Adv. Mater.* **32**, 2001815 (2020).
22. Klimovskikh, I. I. et al. Tunable 3D/2D magnetism in the $(MnBi_2Te_4)(Bi_2Te_3)_m$ topological insulators family. *npj Quant. Mater.* **5**, 54 (2020).
23. Ding, L. et al. Crystal and magnetic structures of magnetic topological insulators $MnBi_2Te_4$ and $MnBi_4Te_7$. *Phys. Rev. B* **101**, 020412 (2020).
24. Vidal, R. C. et al. Topological electronic structure and intrinsic magnetization in $MnBi_4Te_7$: a Bi_2Te_3 derivative with a periodic Mn sublattice. *Phys. Rev. X* **9**, 041065 (2019).
25. Shi, M. Z. et al. Magnetic and transport properties in the magnetic topological insulators $MnBi_2Te_4(Bi_2Te_3)_n$ (n=1, 2). *Phys. Rev. B* **100**, 155144 (2019).
26. He, K. & Xue, Q.-K. The road to high-temperature quantum anomalous Hall effect in magnetic topological insulators. *SPIN* **09**, 1940016 (2019).
27. Cao, L. et al. Growth and characterization of the dynamical axion insulator candidate $Mn_2Bi_2Te_5$ with intrinsic antiferromagnetism. *Phys. Rev. B* **104**, 054421 (2021).
28. Li, H. et al. Antiferromagnetic topological insulator $MnBi_2Te_4$: synthesis and magnetic properties. *Phys. Chem. Chem. Phys.* **22**, 556–563 (2020).
29. Zhao, Y.-F. et al. Even-odd layer-dependent anomalous Hall effect in topological magnet $MnBi_2Te_4$ thin films. *Nano Lett.* **21**, 7691–7698 (2021).
30. Chen, P. et al. Tailoring the hybrid anomalous Hall response in engineered magnetic topological insulator heterostructures. *Nano Lett.* **20**, 1731–1737 (2020).
31. Scholl, A., Liberati, M., Arenholz, E., Ohldag, H. & Stöhr, J. Creation of an antiferromagnetic exchange spring. *Phys. Rev. Lett.* **92**, 247201 (2004).
32. Park, B. G. et al. A spin-valve-like magnetoresistance of an antiferromagnet-based tunnel junction. *Nat. Mater.* **10**, 347–351 (2011).
33. He, K. $MnBi_2Te_4$-family intrinsic magnetic topological materials. *npj Quant. Mater.* **5**, 90 (2020).

34. Awana, G. et al. Critical analysis of proximity-induced magnetism in MnTe/Bi_2Te_3 heterostructures. *Phys. Rev. Mater.* **6**, 053402 (2022).
35. Boltaev, A., Pudonin, F., Sherstnev, I., Egorov, D. & Kozmin, A. Flat magnetic exchange springs as mechanism for additional magnetoresistance in magnetic nanoisland arrays. *J. Magn. Magn. Mater.* **428**, 132–135 (2017).
36. Nogués, J. & Schuller, I. K. Exchange bias. *J. Magn. Magn. Mater.* **192**, 203–232 (1999).
37. Hellwig, O., Kortright, J., Takano, K. & Fullerton, E. E. Switching behavior of Fe-Pt/Ni-Fe exchange-spring films studied by resonant soft-X-ray magneto-optical Kerr effect. *Phys. Rev. B* **62**, 11694–11698 (2000).
38. Khan, M. Y., Shokr, Y. A. & Kuch, W. Coupling of pinned magnetic moments in an antiferromagnet to a ferromagnet and its role for exchange bias. *J. Phys. Condens. Matter* **32**, 075801 (2019).
39. Chi, X. et al. Role of antiferromagnetic bulk exchange coupling on exchange-bias propagation. *Phys. Lett. A* **379**, 2772–2776 (2015).
40. Guo, S. et al. Influence of antiferromagnetic interlayer on the exchange coupling of FM1/AFM/FM2 multilayers. *J. Magn. Magn. Mater.* **344**, 35–38 (2013).
41. Bali, R. et al. Competing magnetic anisotropies in an antiferromagnet-ferromagnet-antiferromagnet trilayer. *J. Appl. Phys.* **106**, 113925 (2009).
42. Rößler, U. & Bogdanov, A. Magnetic phases and reorientation transitions in antiferromagnetically coupled multilayers. *Phys. Rev. B* **69**, 184420 (2004).
43. Wang, Z. et al. Determining the phase diagram of atomically thin layered antiferromagnet $CrCl_3$. *Nat. Nanotechnol.* **14**, 1116–1122 (2019).
44. Yang, S. et al. Odd-even layer-number effect and layer-dependent magnetic phase diagrams in $MnBi_2Te_4$. *Phys. Rev. X* **11**, 011003 (2021).
45. Kneller, E. F. & Hawig, R. The exchange-spring magnet: a new material principle for permanent magnets. *IEEE Trans. Magn.* **27**, 3588–3560 (1991).
46. Fullerton, E. E., Jiang, J. & Bader, S. Hard/soft magnetic heterostructures: model exchange-spring magnets. *J. Magn. Magn. Mater.* **200**, 392–404 (1999).
47. Gruyters, M. & Schmitz, D. Microscopic nature of ferro- and antiferromagnetic interface coupling of uncompensated magnetic moments in exchange bias systems. *Phys. Rev. Lett.* **100**, 077205 (2008).
48. Lu, J. et al. Design and synthesis of an artificial perpendicular hard ferrimagnet with high thermal and magnetic field stabilities. *Sci. Rep.* **7**, 16990 (2017).
49. Meng, L. et al. Anomalous thickness dependence of Curie temperature in air-stable two-dimensional ferromagnetic 1T-$CrTe_2$ grown by chemical vapor deposition. *Nat. Commun.* **12**, 809 (2021).
50. He, Y. et al. Large linear non-saturating magnetoresistance and high mobility in ferromagnetic MnBi. *Nat. Commun.* **12**, 4576 (2021).
51. Butler, W., Zhang, X.-G., Nicholson, D. & MacLaren, J. Spin-dependent scattering and giant magnetoresistance. *J. Magn. Magn. Mater.* **151**, 354–362 (1995).
52. Maranville, B., Ratcliff, W. & Kienzle, P. reductus: a stateless Python data reduction service with a browser front end. *J. Appl. Crystallogr.* **51**, 1500–1506 (2018).
53. Kirby, B. J. et al. Phase-sensitive specular neutron reflectometry for imaging the nanometer scale composition depth profile of thin-film materials. *Curr. Opin. Colloid Interface Sci.* **17**, 44–53 (2012).
54. Blöchl, P. E. Projector augmented-wave method. *Phys. Rev. B* **50**, 17953–17979 (1994).
55. Kresse, G. & Furthmüller, J. Efficient iterative schemes for ab initio total-energy calculations using a plane-wave basis set. *Phys. Rev. B* **54**, 11169–11186 (1996).
56. Kresse, G. & Joubert, D. From ultrasoft pseudopotentials to the projector augmented-wave method. *Phys. Rev. B* **59**, 1758–1775 (1999).
57. Perdew, J. P., Burke, K. & Ernzerhof, M. Generalized gradient approximation made simple. *Phys. Rev. Lett.* **77**, 3865–3868 (1996).
58. Anisimov, V. I., Zaanen, J. & Andersen, O. K. Band theory and Mott insulators: Hubbard U instead of Stoner I. *Phys. Rev. B* **44**, 943–954 (1991).
59. Dudarev, S. L., Botton, G. A., Savrasov, S. Y., Humphreys, C. & Sutton, A. P. Electron-energy-loss spectra and the structural stability of nickel oxide: an LSDA+U study. *Phys. Rev. B* **57**, 1505–1509 (1998).
60. Klimeš, J., Bowler, D. R. & Michaelides, A. Van der Waals density functionals applied to solids. *Phys. Rev. B* **83**, 195131 (2011).
61. Lado, J. L. & Fernández-Rossier, J. On the origin of magnetic anisotropy in two dimensional CrI_3. *2D Mater.* **4**, 035002 (2017).

Acknowledgements

This work is sponsored by the National Key R&D Program of China under contract no. 2017YFA0305400, the National Natural Science Foundation of China (grants nos. 61874172 and 11904230), the Major Project of Shanghai Municipal Science and Technology (grant no. 2018SHZDZX02), the Shanghai Engineering Research Center of Energy Efficient and Custom AI IC, and the Shanghaitech Quantum Device and Soft Matter Nano-fabrication Labs (SMN180827). X.K. acknowledges support from the Merck POC programme and the Shanghai Rising-Star programme (grant no. 21QA1406000). Y.Y. acknowledges support from Shanghai Pujiang Program (grant no. 20PJ1411500). We acknowledge the facilities, and scientific and technical assistance, of the Australian Microscopy & Microanalysis Research Facility at the Centre for Microscopy and Microanalysis, The University of Queensland. Q.Y. acknowledges support from the Shanghai Sailing Program (grant no. 19YF1433200). We would also like to thank the ISIS neutron facility for the award of beam time (RB2000244, https://doi.org/10.5286/ISIS.E.RB2000244). Certain commercial equipment is identified in this paper to foster understanding. Such identification does not imply recommendation or endorsement by NIST. Diamond Light Source is acknowledged for the beam time allocated on I10 under proposal MM30262. B.A. and T.H. acknowledge funding from the Engineering and Physical Sciences Research Council (EP/N032128/1). F.X. was supported by the National Natural Science Foundation of China (52225207 and 52150103), the Shanghai Municipal Science and Technology Major Project (grant no. 2019SHZDZX01), the Program of Shanghai Academic/Technology Research Leader (grant no. 20XD1400200) and the Shanghai Pilot Program for Basic Research—FuDan University 21TQ1400100 (21TQ006).

Author contributions

X.K. and Q.Y. conceived and supervised the study. P.C. and S. Liu grew the samples. P.C., J.L. and P.H. performed the characterization measurements and conducted the transport measurements. Q.Y. and P.C. analysed the transport and characterization data. P.C. and Y.Y. conducted the macro-spin simulations. J.X. and H.Z. contributed the first-principles calculations. Q.S., A.L., X.H. and J.Z. performed the transmission electron microscopy characterization. A.J.G., P.Q., P.P.B., C.J.K., A.J.C. and S. Langridge performed the neutron reflectometry measurements. B.A., E.H. and T.H. performed X-ray magnetic circular dichroism measurements, and S. Liu, B.C., G.Y. and F.X. performed superconducting quantum interference device measurements. Y.J. and Z.L. performed the angle-resolved photoemission spectroscopy measurements. P.C., Q.Y., Y.Y. and X.K. wrote the manuscript. All authors discussed the results and commented on the manuscript.

Competing interests

The authors declare no competing interests.

Additional information

Supplementary information The online version contains supplementary material available at https://doi.org/10.1038/s41928-022-00880-1.

Correspondence and requests for materials should be addressed to Qi Yao, Yumeng Yang or Xufeng Kou.

Peer review information *Nature Electronics* thanks Xianhui Chen and the other, anonymous, reviewer(s) for their contribution to the peer review of this work.

[1]School of Information Science and Technology, ShanghaiTech University, Shanghai, China. [2]Shanghai Institute of Microsystem and Information Technology, Chinese Academy of Sciences, Shanghai, China. [3]University of Chinese Academy of Science, Beijing, China. [4]ShanghaiTech Laboratory for Topological Physics, ShanghaiTech University, Shanghai, China. [5]School of Physical Science and Technology, ShanghaiTech University, Shanghai, China. [6]National Laboratory of Solid-State Microstructures, School of Physics, Nanjing University, Nanjing, China. [7]School of Mechanical and Mining Engineering, The University of Queensland, Queensland, Queensland, Australia. [8]Centre for Microscopy and Microanalysis, The University of Queensland, St Lucia, Queensland, Australia. [9]NIST Center for Neutron Research, National Institute of Standards and Technology, Gaithersburg, MD, USA. [10]ISIS-Neutron and Muon Source, Rutherford Appleton Laboratory, Didcot, UK. [11]Institute of Microstructure and Property of Advanced Materials, Beijing University of Technology, Beijing, China. [12]Department of Physics, Clarendon Laboratory, University of Oxford, Oxford, UK. [13]State Key Laboratory of Surface Physics, Department of Physics, Fudan University, Shanghai, China. [14]Songshan Lake Materials Laboratory Dongguan, Guangdong, China. [15]Beijing National Laboratory for Condensed Matter Physics Institute of Physics Chinese Academy of Sciences, Beijing, China. [16]Collaborative Innovation Center of Advanced Microstructures, Nanjing University, Nanjing, China. [17]These authors contributed equally: Peng Chen, Qi Yao. ✉e-mail: yaoqi@shanghaitech.edu.cn; yangym1@shanghaitech.edu.cn; kouxf@shanghaitech.edu.cn